

Structural and optical properties of sol gel processed nanopowders of lead doped $Y_2Ti_2O_7$ pyrochlore

Moulay Mustapha Yahyaoui^a, Karoum Limame^{a,b}, Salaheddine Sayouri^{a,*}, Boujamaâ Jaber^c and Larbi Laanab^d

^aLaboratoire de Physique Théorique et Appliquée, Faculté des Sciences Dhar Mehraz, B.P. 1796, Fès-Atlas, Fès. Morocco.

^bCentre Régional des Métiers de l'Éducation et de la Formation (CRMEF) de Fès, B. P. 49, Fès. Morocco.

^cCentre National pour la Recherche Scientifique et Technique (CNRST), Angle, B. P. 8027 Nation Unies Rabat Morocco.

^dLaboratoire Conception et Système (LCS), Faculté des Sciences Rabat, B.P. 1014 RP, Rabat Morocco

To investigate the annealing temperature and stoichiometry effects, on crystal growth and optical properties of lead doped yttrium titanate, we prepared the stoichiometric samples: $Y_{2(1-x)}Pb_{2x}Ti_2O_{7-\delta}$, where $x = 0, 10, 20, 30$ and 40% (YPTx), using the sol gel method. Phase transformations in the samples were followed by X-ray diffraction (XRD), Raman and UV-Vis spectroscopies, and transmission electron microscopy. XRD analysis shows that the undoped sample exhibits the pyrochlore structure with an unit cell parameter of 10.096 \AA , with few traces of the TiO_2 rutile phase. Moreover, coexisting $Y_2Ti_2O_7$, $PbTi_3O_7$ and $PbTiO_3$ phases, depending on $x(Pb^{2+})$, are observed; all these phases are stable in the corresponding range of Pb^{2+} concentration. The reflectance UV-vis spectra show the presence of a fundamental band in pure and doped samples, assigned to the pure phase $Y_2Ti_2O_7$, and a defect band in YT and YPT10; the latter may be assigned to a Frenkel-pair associated with cation defects.

Key words: Pyrochlore-type yttrium titanate ($Y_2Ti_2O_7$), Sol-gel, Optical properties, X-ray diffraction.

Introduction

Pyrochlore oxides of general formula $A_2B_2O_7$ are of great interest from both theoretical and experimental points of view. The structure of $A_2B_2O_7$ is closely related to those of fluorite and can be considered as an ordered, defective fluorite structured materials with anion vacancies [1,2]. In addition, these oxides permit a wide variety of substitution at the A and B sites when the ionic radius ratio (R_A/R_B) and charge neutrality criteria are satisfied; the ratio R_A/R_B plays a major role in structural disorder in pyrochlores [3, 4]. The phase transition from the pyrochlore structure to the ideal defect fluorite structure is an order-to-disorder transition, hence the order-disorder transformation takes place in both the anion and cation arrangements. This disorder may be introduced into the structure by different effects: compositional changes, heat treatment, etc.

$Y_2Ti_2O_7$ pyrochlore material has attracted considerable attention for its potential applications, such as n-type semi-conductors and photocatalysts [5-7]. Indeed, this material can be used in devices such as sensors and transistors [8], dielectrics and fast conductors [5, 9] and as a host material for immobilization of nuclear solid waste [10, 11] and can be used as solid electrolyte in solid-oxide fuel cells [12]. This material has been

synthesized by different methods [13-17]. On the other hand, doping of this material by aliovalent, in A site, improves its ionic or/and electrical conductivity by the creation of oxygen vacancies as charge compensators [6, 18], and by the formation of the anion Frenkel defect [6, 19, 20].

In a previous work [21] we have prepared a series of Pb^{2+} doped $Y_2Ti_2O_7$ pyrochlore nanoparticles ($Y_{2(1-x)}Pb_{2x}Ti_2O_{7-\delta}$, where $x=0, 10, 20, 30$ and 40% (YPTx)) by the sol-gel method, that were heat treated at 800°C for 2hrs. The results showed that no structural change occurred in YPTx at 10% ; however, starting from 20% , the formation of the $PbTiO_3$ phase in pseudo-cubic symmetry along with $Y_2Ti_2O_7$ phase was observed, with no evidence of other secondary phases for all the samples.

In the present paper, we study the effect of the stoichiometry and the annealing temperature on solubility of Pb^{2+} in $Y_2Ti_2O_7$, on growth of crystalline structure and on stability and optical band gaps of the produced samples. In this aim, using the sol-gel process, we synthesized nanoparticles of the Pb^{2+} doped $Y_2Ti_2O_7$ with the composition $Y_{2(1-x)}Pb_{2x}Ti_2O_{7-\delta}$, where $x = 0, 10, 20, 30$ and 40% (YPTx). During the preparation of the samples and first experimental characterizations, we have observed that the samples show new features when the annealing temperature is increased to 900°C (in the previous work this temperature was 800°C) which are signaled in the paper; and which enables a detail analysis of results.

*Corresponding author:
Tel : +212-6-73-78-52-88
Fax: +212-5-35-73-33-49
E-mail: ssayouri@gmail.com

The samples have been investigated using X-ray diffraction (XRD) and Raman spectroscopy to identify the structural transformation, the transmission electron microscopy (TEM) to obtain information about the size and the microstructure of the samples, and UV-Vis spectroscopy in order to show the correlation between the band gap and the structural feature of the materials.

Experimental Details

The ceramic samples YPT x , with $x = 0$ (YT), 10, 20, 30 and 40%, were prepared by the sol-gel method through the destabilization of colloidal solution (DCS). In comparison to the traditional methods, the sol gel process offers several advantages, namely, low processing temperature, high purity, homogeneity and an excellent control of the stoichiometry of the products [22].

YPT x powders were fabricated in two steps. The first step consisted in the preparation of a colloidal solution of TiO_2 . Titanium alkoxide was added to lactic acid aqueous solution. A white precipitate was then obtained under stirring at 80 °C, for 12 hrs, which transforms into clear solution. In a second step, lead and yttrium acetates were added to the latter colloidal solution, in stoichiometric amounts. Under rigorous magnetic stirring and slow heating (40 °C), the yttrium acetate was dispersed in a spot of distilled water and then concentrated nitric acid was added drop to drop, to ensure complete acetate dissolution. An excess of lead acetate (5%) was added to compensate the possible lead loss throughout the various manufacturing steps. The xerogel obtained was annealed, in static air, at 900 °C, with a heating rate of 5°C/min and a dwelling time of 2hrs.

Results and Discussion

Structural description

$A_2B_2O_7$ phase adopts a cubic symmetry with the space group $Fd-3m$; $Z = 8$; it can be considered to be derived from the fluorite structure (CaF_2) by removing

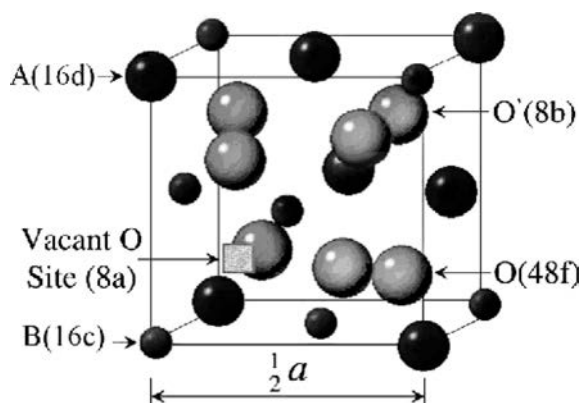


Fig. 1. Schematic view of one-eighth of unit cell of pyrochlore structure.

one-eighth of the anions so that the composition can be written as $A_2B_2O_7V_a$ where V_a is the anion vacancy [23-25]. In the pyrochlore structure, there are two kinds of oxygen ions, O and O'. The trivalent A^{3+} cations are surrounded by eight oxygen anions ($6O+2O'$) forming a distorted cubic site (16d). The tetravalent B^{4+} cations have six nearest neighbors (O) which form a distorted octahedral site (16c). The 48f tetrahedral sites consist of O anions as "central atom, two A cations and two B cations as apexes, while the 8b tetrahedral sites are constituted by O' anions surrounded by four A cations (Fig. 1). Besides, pyrochloreIF structure contains vacant 8a tetrahedral sites with four B cations as apexes [23, 26].

XRD analysis

X-Ray diffraction (XRD) patterns of various samples, annealed at 900 °C for 2 hrs, are shown in Fig. 2.

In Fig. 2(a), we observe that the undoped sample (YT) crystallizes in the $Y_2Ti_2O_7$ (Y) pyrochlore phase, (JCPDS 01-070-7158) together with a small amount of the TiO_2 (T) rutile phase (JCPDS 01-089-8300). This behavior is well reported in the literature [7, 14, 27] when reagents are taken in stoichiometric amounts. The estimated lattice parameter of this pyrochlore phase was $a=10.096$ Å; this value is in good agreement with those reported by other authors [4, 5, 28, 29].

When $x(Pb^{2+})$ has been introduced in YT, several diffraction peaks appeared, depending of $x(Pb^{2+})$, indicating the presence of several crystalline phases. All peaks of X-ray diffraction were matched with JCPDS of various coexisting phases in each sample. In addition, we observed the decrease in the intensity of the peaks of the pyrochlore phase ($Y_2Ti_2O_7$), with the doping increase.

Fig. 2(b), related to YPT10, shows the increase of intensities of the peaks of the TiO_2 rutile phase, and the emergence of small diffraction peaks at $2\theta = 28.70$; 30.19 ; 30.90 and 47.49 related to the secondary phase $PbTi_3O_7$ (P) (JCPDS 01-070-1016). It is important to note the absence of $PbTiO_3$, which indicates that the limit of solubility of Pb^{2+} in $Y_2Ti_2O_7$ is larger as 10%. Starting from 20% of $x(Pb^{2+})$, we can observe the presence of the $Y_2Ti_2O_7$ pyrochlore phase, the $PbTi_3O_7$ phase and the disappearance of TiO_2 . In the spectrum of YPT20 (Fig. 2(c)), other peaks related to $PbTi_3O_7$ are observed and several peaks related to the perovskite phase $PbTiO_3$ (PT) in tetragonal symmetry ($c/a = 1.04$) appeared, in particular, the principal one emerges at $q = 31.68$; this result indicates that the limit of solubility of Pb^{2+} in $Y_2Ti_2O_7$ is smaller than 20% which confirms our previous work [21].

When $x(Pb^{2+})$ is increased, some other peaks related to $PbTiO_3$ appear in YPT30% (Fig. 2(d)) and the intensities of the peaks related to $PbTi_3O_7$ phase increased. In YPT40% (Fig. 2(e)), the amount of the tetragonal $PbTiO_3$ phase is more prominent in comparison to the $PbTi_3O_7$

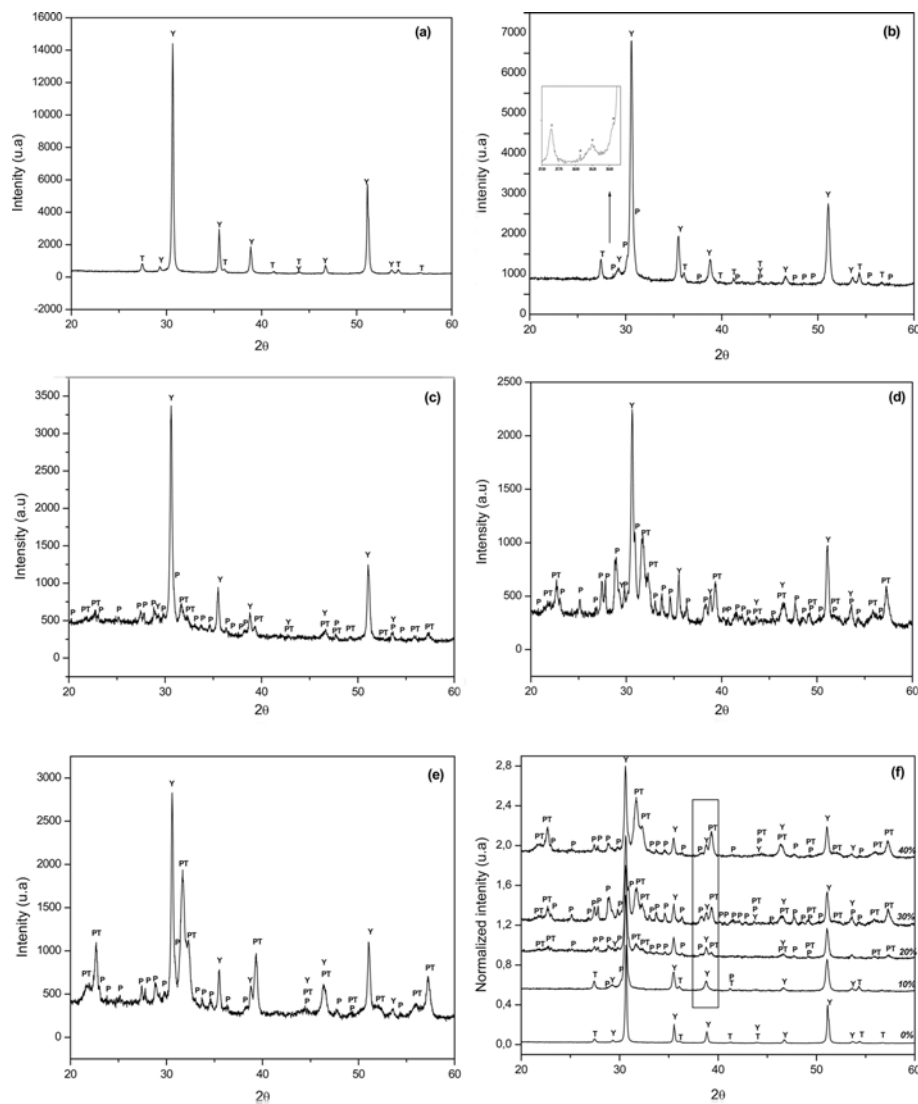


Fig. 2. X-ray diffraction patterns of (a) YT, (b) YPT10, (c) YPT20, (d) YPT30, (e) YPT40 and (f) YPTx annealed at 900 °C.

Table 1. Percentages and crystalline phases of different ceramic samples in the system YPTx annealed at 900°C.

Ceramic code	Time of Calcinations	Heating rate (°C)	Crystalline phases
YT	2 h	5 min	Y(95%)+T(5%)
YPT10	2 h	5 min	Y(86%)+T(10%)+P(4%)
YPT20	2 h	5 min	Y(68%)+P(17%)+PT(15%)
YPT30	2 h	5 min	Y(52%)+P(24%)+PT(24%)
YPT40	2 h	5 min	Y(50%)+P(16%)+PT(34%)

Y:Y₂Ti₂O₇, T:TiO₂, P:PbTi₃O₇, PT:PbTiO₃.

phase, which is confirmed by the relative intensity of XRD lines of Y₂Ti₂O₇, PbTi₃O₇ and PbTiO₃ phases, as illustrated in Fig. 2(f) (e.g.see peaks around 2q=38.5).

The relative amount, wt(i)%, of the coexisting phases in each sample was estimated, from XRD patterns, using the semi empirical equation [30].

$$wt(i)\% = \frac{I_i}{I_Y + I_T + I_P + I_{PT}} \times 100 \quad (1)$$

Where I_i is the intensity of the principal peaks of the different coexisting phases in each sample ($i=Y(Y_2Ti_2O_7)$, $T(TiO_2)$, $P(PbTi_3O_7)$ and $PT(PbTiO_3)$). The obtained results are gathered in Table 1.

The crystallite size, D , of the coexisting phases in each sample was estimated using Scherrer's equation

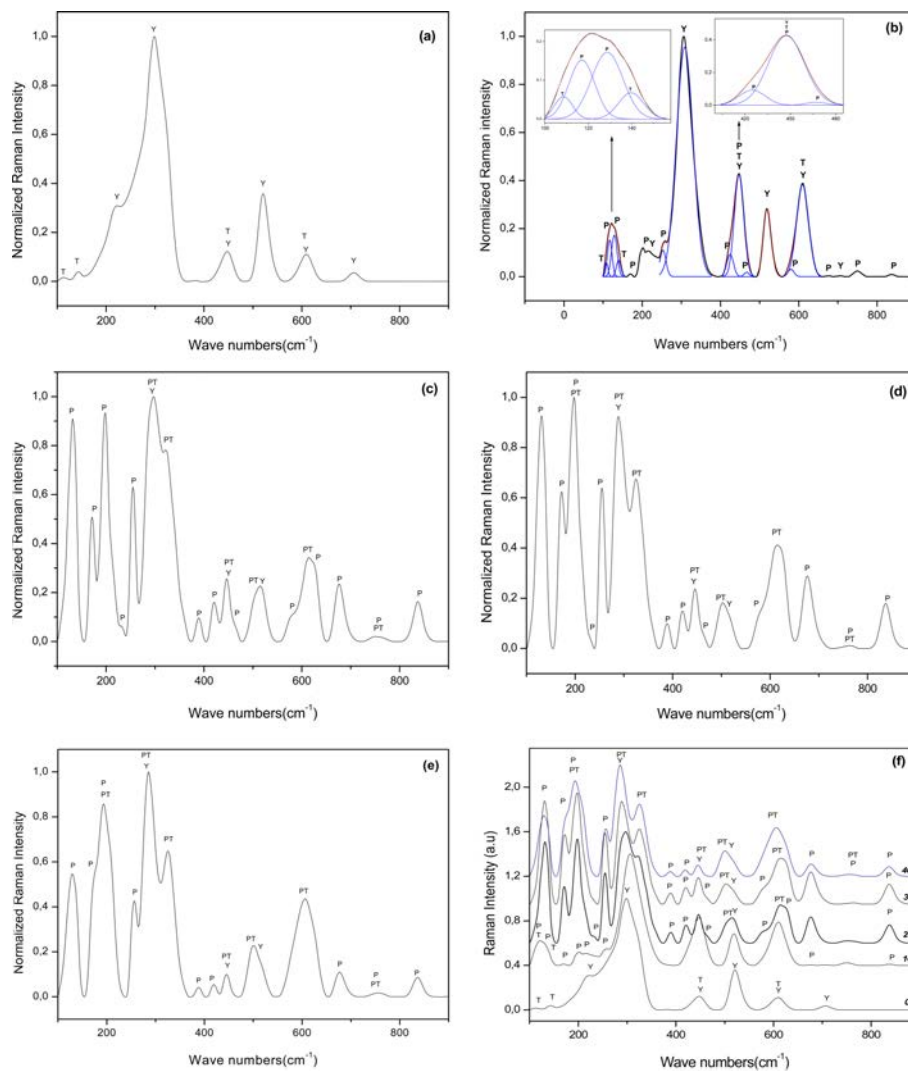
$$D = \frac{0.9\lambda}{\beta \cos\theta} \quad (2)$$

where λ is the X-ray wavelength (1.5406 Å), β is the full-width-at-half-maximum (FWHM) of a characteristic diffraction peak and θ the diffraction angle (the value is calculated from FWHM of the most intense line at the diffraction angle). Values of D and lattice parameters for the crystalline phases in the YPTx samples are gathered in Table 2.

It is reported [15] that the higher ionic radius of the dopant increases the lattice parameter; this explains the observed increase in the lattice parameter within incorporation of the dopant. The crystallite size of Y₂Ti₂O₇

Table 2. Unit cell parameter of $Y_2Ti_2O_7$ and crystallite size of different coexisting phases in YPTx annealed at 900°C. The last column of the Table gives the value found for YT by Singh et al. [29].

YPTx	Lattice Parameter of $Y_2Ti_2O_7$ (Å)	Crystallite size of $Y_2Ti_2O_7$ (nm)	Crystallite size of TiO_2 (nm)	Crystallite size of $PbTi_3O_7$ (nm)	Crystallite size of $PbTiO_3$ (nm)	Crystallite size of $Y_2Ti_2O_7$ (nm) [29]
YT	10.096	86	32	–	–	≈ 87
YPT10	10.110	75	30	129	–	–
YPT20	10.109	78	–	127	33	–
YPT30	10.109	77	–	122	35	–
YPT40	10.110	79	–	118	38	–

**Fig. 3.** Raman spectrum of (a) YT, (b) YPT10 (convoluted), (c) YPT20, (d) YPT30, (e) YPT40 and (f) YPTx annealed at 900 °C.

in the undoped sample is the same as that found by Singh et al. [29] (Table 2). From Table 2, it is observed that for the doped samples, the lattice parameter of $Y_2Ti_2O_7$ and the crystallite size related to different coexisting crystalline phases remain practically constants when doping increases. The same behavior was observed in Ca^{2+} doped $Y_2Ti_2O_7$ [12].

In comparison to YPTx (pure and doped) heated at 800 °C [21], the crystallite size is larger in samples treated at 900 °C. However, the lattice parameter of

$Y_2Ti_2O_7$ decreases, which may be due to the effect of the crystallization temperature. These results are in good agreement with others reported in the literature [16, 31].

Furthermore, comparatively to doped YPTx heated at 800 °C [21], the structure of the doped samples heated at 900 °C for 2hrs, reveals the presence in all samples of the secondary phase $PbTi_3O_7$, and the $PbTiO_3$ structure changes from pseudo cubic to tetragonal phase with a tetragonality $c/a = 1.04$. This structural change in lead

titanate perovskite phase was reported as being due to the effect of the increase of the crystallite size [32]. Aykan [33] has found the PbTi_3O_7 as a novel compound by the reaction between PbO and TiO_2 in the TiO_2 -rich region. Gelabert et al. [34] reported that the existence of TiO_2 or/and PbTi_3O_7 or/and PbTiO_3 depends on Pb/Ti ratio. When the amount of Pb^{2+} increases, the PbTi_3O_7 and TiO_2 ; PbTi_3O_7 and PbTiO_3 ; PbTiO_3 and PbO phases appear in this order.

In our case, we have found the same order of emergence of phases. Indeed, the incorporation of 10% of Pb^{2+} in YT has given rise to an increase of TiO_2 and appearance of PbTi_3O_7 (Table 1). As the Pb^{2+} content increases the ratio Pb/Ti increases, showing the coexistence of the PbTi_3O_7 and PbTiO_3 phases and the disappearance of TiO_2 in YPT20% and YPT30%. In YPT40% the Pb^{2+} content becomes important, giving rise to the predominance of PbTiO_3 with respect to PbTi_3O_7 (Table 1). The multiphase nature of the samples as identified by XRD can also be seen in the excitations of these lattices, i.e. via the Raman spectra of the samples.

Raman analysis

The Raman spectrum of the pure sample (YT) heated at 900°C for 2hrs is shown in Fig. 3(a). Group theory analysis shows that there are only six Raman active modes in $\text{A}_2\text{B}_2\text{O}_7$ pyrochlore compounds, having space group (Fd3m, Z=8) [35, 36]

$$\Gamma=(\text{A}_{1g}+\text{E}_g+4\text{F}_{2g}) \quad (3)$$

These modes arise due to vibrations of oxygen atoms, since A and B cations do not contribute to active Raman bands because they possess centrosymmetric symmetry with an inversion centre. Oxygen atoms located at the 48f positions contribute to five phonon modes ($\text{A}_{1g} + \text{E}_g + 3\text{F}_{2g}$), whereas those located in 8b, give a single F_{2g} mode [27].

The estimated frequencies of the active modes (Table 3), corresponding to samples heat treated at 900°C , are in good agreement with those reported by Garbout et al. [13], however slight shifts of the main vibrational frequencies ($\approx 299 \text{ cm}^{-1}$) are observed, when compared

to other authors [4, 16, 37, 38].

For the pure sample (Fig. 3(a)), as the bond length of Ti-O is shorter than that of Y-O , we can assign the modes at 447 and 609 cm^{-1} , related to $\text{Y}_2\text{Ti}_2\text{O}_7$, to the symmetric and to asymmetric Ti-O stretching vibrations respectively [13, 39]; the latter are due to the vibrations of atoms inside the TiO_6 octahedra.

Compared with other published results [4, 29, 38], the Ti-O stretching mode exhibited an increase in intensity due to the presence of TiO_2 rutile phase in this sample; this behavior was also observed by Garbout et al.[40]. The band at 143 cm^{-1} is assigned to the E_g mode of the TiO_2 rutile phase [40], which is supported by the presence of TiO_2 as shown by XRD analysis (Fig. 2(a)).

The mode at 223 cm^{-1} is due to the distortion of the TiO_6 octahedron [36]. The most intense Raman-active mode at 299 cm^{-1} , which consists of two modes (E_g , F_{2g}) with very similar frequencies, is attributed to O-Y-O bending mode. Another intense band observed at about 520 cm^{-1} corresponds to A_{1g} and may be attributed to Y-O stretching. The broad band at 706 cm^{-1} may be the fourth F_{2g} mode. The appearance of another peak around 112 cm^{-1} may be due to the nanosized grain of TiO_2 rutile [41, 42].

The Raman spectra of doped YPTx samples, with $x = 10, 20, 30$, and 40 (%), heated at 900°C for 2 hrs are shown in Fig 3(b-f).

To reveal the overlap of the Raman active modes related to different coexisting phases in doped samples, we have deconvoluted the bands of Raman spectra (e.g. Fig. 3(b)). The results are summarized in Table 4.

When Pb^{2+} is gradually incorporated in the structure, a slight shift of the vibrational frequencies, a decrease of the peak intensities ($\approx 308 \text{ cm}^{-1}$; $\approx 520 \text{ cm}^{-1}$), and disappearance of the mode at 706 cm^{-1} of $\text{Y}_2\text{Ti}_2\text{O}_7$ are observed, which confirms that the phase fraction gradually decreases as the doping is increased, as observed in XRD spectra (Fig. 2(f)) and Table 1).

As shown in the spectrum related to YPT10 (Fig. 3(b)), in addition to the presence of Raman modes of $\text{Y}_2\text{Ti}_2\text{O}_7$, the Ti-O stretching modes of TiO_2 rutile exhibited an increase in intensity and other Raman active modes appeared at 117 ; 129 ; 170 ; 201 ; 252 ; 676 ;

Table 3. Comparison of Raman spectra frequencies of $\text{Y}_2\text{Ti}_2\text{O}_7$ annealed at $T=900^\circ\text{C}$ with the literature.

This work	Garbout et al. [13]	Fuentes et al. [16]	Glerup et al. [4]	Garbout et al. [37]	Bouattour et al. [38]	Raman mode
706	700	712	720	708	695	F_{2g}
609	608	588	609		609	F_{2g}
520	514	523	522	524	519	A_{1g}
447	447	451	448	457	448	F_{2g}
		328		328		
299	299	308	333	310	311	$\text{F}_{2g} + \text{E}_g$
223	230	220	221	222	206	–

Table 4. Raman frequencies of YPTx compounds annealed at T = 900 °C for 2 hrs.

YT		YPT10			YPT20			YPT30			YPT40		
Y	T	Y	T	P	Y	P	PT	Y	P	PT	Y	P	PT
	112		108										107
				117		124			118			119	
				129		134			130			130	
										139			139
	143		140										
				170		171			172			171	
				201		197			197			191	
													210
223		218			232			232					
				252		255			254			256	
							289			288			282
299		308			304			302			295		
						320	320		325	325		326	326
						329	329						
						390			389			388	
				424		420			420			419	
447	447	447	447	447	446	446	446	445	445	445	445	445	445
				467		465			465				
							500			500			498
520		519			516			519			517		
				580		580			579				
609	609	610	610										
							612			610			606
						629			628				
				676		676			676			676	
706		705											
				749		749			764				
				836		837			837			837	

749 and 836 cm^{-1} ; these modes were reported as related to the PbTi_3O_7 phase [43]. The deconvolution of the band centered at 130 cm^{-1} (e.g.) shows the coexistence of the bands related to TiO_2 and PbTi_3O_7 .

The spectrum of YPT20 (Fig. 3(c)) shows the disappearance of Raman active modes related to the TiO_2 rutile phase (absence of the mode at 143 cm^{-1} (Specific peak of phase)), and also an enhancement in intensities of those of the PbTi_3O_7 secondary phase, with the appearance of the small Raman active modes assigned to tetragonal PbTiO_3 phase, such as modes at 288, 500 and at 612 cm^{-1} [44, 45]. This result indicates the close correspondence between Raman spectrum and XRD (Fig. 2(c)). The intensities of the peaks related to PbTi_3O_7 and PbTiO_3 phases become more intense in YPT30 Raman spectrum (Fig. 3(d)), and their masked active Raman modes, such as the peak at 288 cm^{-1} for PbTiO_3 and that at 420 cm^{-1} for PbTi_3O_7 , appear clearly.

As the dopant concentration content increases (YPT40 (Fig. 3(e))), some active Raman modes ascribed to PbTi_3O_7 phase disappear leaving the place to other active Raman modes related to PbTiO_3 phase.

This indicates that when the Pb^{2+} content is important, the perovskite phase becomes dominant as compared to PbTi_3O_7 ; this result is consistent with those of XRD illustrated in Fig. 2(e-f) and Table 1.

Comparatively to YPTx annealed at 900 °C, the Raman spectra related to YPTx annealed at 800 °C [21] show clearly the presence of PbTiO_3 for $x > 10\%$ and the absence of PbTi_3O_7 in YPTx.

TEM analysis

Transmission Electron Microscopy (TEM) was employed to obtain direct information on the size and the morphology of the prepared YPTx nanocrystals. TEM results are shown in Fig. 4(a-c). From these Figures, it can be observed the presence of a distribution of quasi-spherical nanoparticles with a good dispersion and different sizes.

These images show a dispersion of the grains, and one can clearly distinguish the presence of agglomerates. Indeed, Fig. 4(a), related to YT, reveals average grain sizes around 71 nm and 37 nm; grains given in Fig. 4(b), related to YPT10, have sizes around 30 nm, 70 nm and 120 nm, and for YPT20 (Fig. 4(c)) the particle

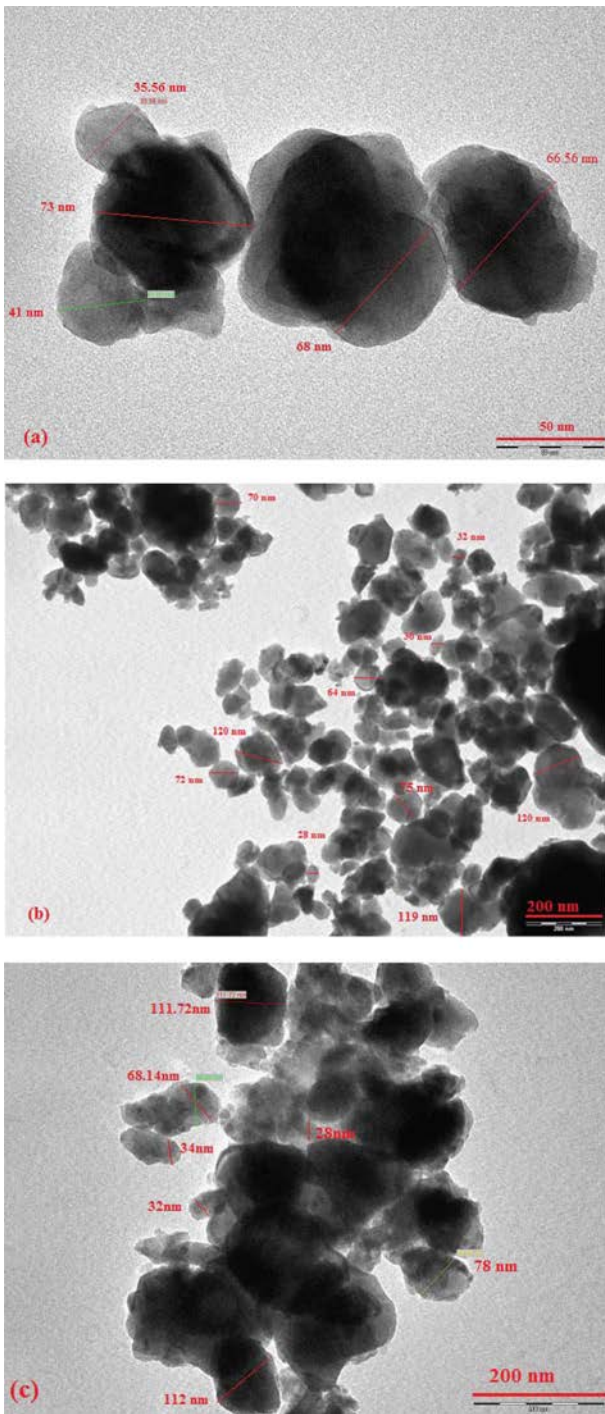


Fig. 4. Transmission electron micrographs of (a) YT, (b) YPT10 and (c) YPT20 annealed at 900 °C for 2 hrs.

sizes are around 30 nm, 73 nm, and 112 nm.

UV-Vis diffuse reflectance spectra and band gap energy

UV-Vis investigations of the samples treated at 900 °C were carried out for wavelengths varying from 200 nm up to 800 nm. Diffuse reflectance spectra of different samples are shown in Fig. 5.

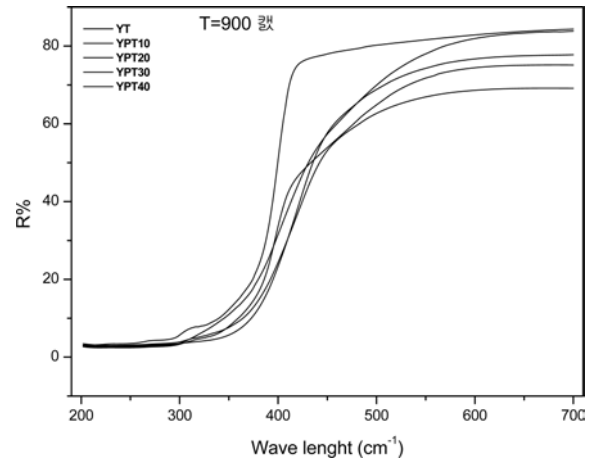


Fig. 5. UV-vis reflectance spectra of YPTx annealed at 900 °C.

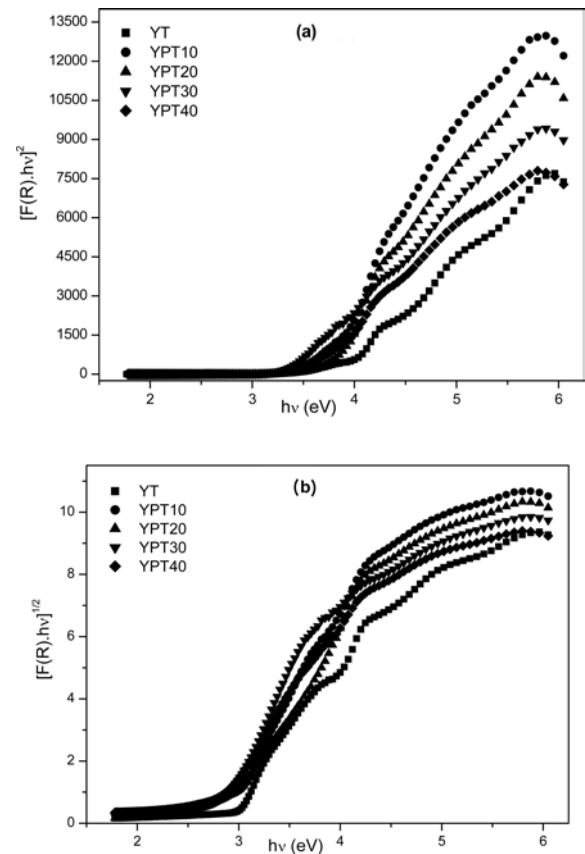


Fig. 6. Tauc-plots calculated from the UV-vis diffuse reflectance for band gap energy calculations of direct gap (a) and indirect gap (b) of YPTx annealed at 900 °C.

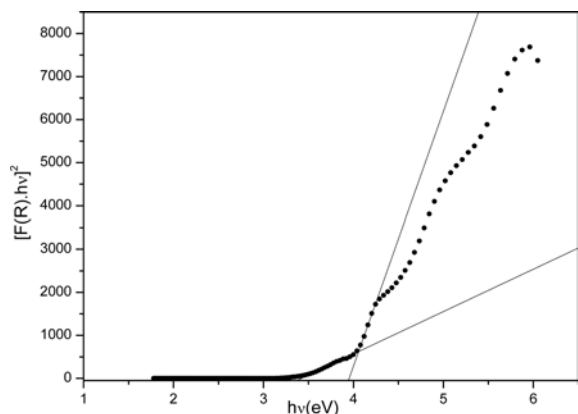
In order to quantify the effect of lead on direct band gap energy on YT, we have calculated the remission function, using the Kubelka–Munk transformation [31, 38, 46, 47] of UV-Vis diffuse reflectance (R) spectra

$$F(R) = (1-R)^2/2R \tag{4}$$

The intersection between the linear fit of the plot

Table 5. Band gap energy of YPTx compounds annealed at $T = 900\text{ }^\circ\text{C}$ for 2 hrs.

YPTx	Direct band gap energy (eV)	Indirect band gap energy (eV)
YT	3,90	2,96
YPT10	3,85	2,87
YPT20	3,84	2,75
YPT30	3,32	2,84
YPT40	3,73	2,77

**Fig. 7.** Tauc-plots calculated for direct band gap and band defect energies calculations of YT annealed at $900\text{ }^\circ\text{C}$.

$(F(R).hv)^2$ and $(F(R).hv)^{1/2}$ versus $h\nu$ with the photon energy axis gives the value of direct and indirect band gap respectively (Fig. 6(a-b)).

The diffuse reflectance spectra are characterized by the presence of a main or fundamental band. The obtained results corresponding to direct and indirect band gap for all samples are listed in Table 5. The estimated value of direct band gap of YT (Fig. 7) is slightly high than what is reported in the literature for the pure $Y_2Ti_2O_7$ [26, 29, 31]. The obtained value of indirect band gap for the pure $Y_2Ti_2O_7$ was about 2,96 eV consistent with calculated value 2.87 eV reported by Terki et al. [48].

Furthermore, the values of the direct and indirect band gap of doped samples are respectively in the range 3.32-3.90 eV and 2.75-2.96 eV (Table 5) which may be attributed to the band gap of the dominant phase ($Y_2Ti_2O_7$).

One can also observe the presence of a defect band in YT (Fig. 5) and YPT10 spectra. The corresponding gap energies are 3.42 eV and 3.43 eV, respectively. This defect band disappears for $x > 10$ (Fig. 5). The calculated energy of Frenkel pairs creation and of this pair creation with defect cation equals 4.6 eV [26] and 3.8 eV [49] respectively in a pure $Y_2Ti_2O_7$ oxide, for this consideration, this band may be assigned to a Frenkel-pair associated with cation defects. Indeed it is reported that the Frenkel pair can be due to anionic disorder created into the pyrochlore network: 48f oxygen vacancies and interstitial oxygen on 8a sites

can be associated; oxygen atoms migrate from 48f site to 8a site.

The substitution of Y^{3+} with lower valence cation, Pb^{2+} in our case, causes an electronic unbalance that can be compensated by the formation of rutile TiO_2 phase, which is more pronounced in YPT10 as observed on XRD spectra (Fig. 2(a-b), and Table 1), and not by the generation of oxygen vacancies, indeed the amount of TiO_2 increases and the Frenkel pair energy remains practically constant.

Conclusions

Lead doped yttrium titanate nanoparticles were prepared by the sol-gel process, and heat treated at $900\text{ }^\circ\text{C}$ for 2 h. X-Ray diffraction analysis shows that the undoped sample exhibits the pyrochlore structure, with few traces of the TiO_2 rutile phase. When the doping increases, a coexistence of $Y_2Ti_2O_7$, $PbTi_3O_7$ and $PbTiO_3$ phases, depending on $x(Pb^{2+})$ is observed. The $PbTiO_3$ phase emerges at 20% which confirms that the limit of solubility of Pb^{2+} in $Y_2Ti_2O_7$ is smaller than 20%. These results are consistent with those of Raman spectroscopy results.

Below 20% of lead content, the crystallite size decreases and the lattice parameter increases with doping, and then becomes practically constant from this value. TEM micrographs show a distribution of quasi-spherical nanoparticles with different sizes.

UV-Visible reflectance spectra results of YPTx revealed the existence of a fundamental band for the pure and doped samples, and a defect band, assigned to Frenkel-pair associated with cation defects; the latter is observed for the YT and YPT10 samples and disappears for $x > 10$.

References

1. E.E. Erickson, D. Gray, K. Taylor, R.T. Macaluso, L.A. Letard, G.S. Lee, J.Y. Chan, Mater. Res. Bull. 37 (2002) 2077-2083.
2. C.R. Stanek, L. Minervini, R.W. Grimes, J. Am. Ceram. Soc. 85 (2002) 2792-2798.
3. B.P. Mandal, N. Garg, S. M. Sharma, A. K. Tyagi, J. Solid State Chem., 179 (2006) 512-521.
4. M. Glerup, O.F. Nielsen, F.W. Poulsen, J. Solid State Chem. 160 (2001) 25-32.
5. M.A. Subramanian, G. Aravamudan, G.V.S. Rao, Prog. Solid State Chem. 15 (1983) 55-143.
6. N. Kim, C.P. Grey, Dalton Trans. 19 (2004) 3048-3052.
7. M. Higashi, R. Abe, K. Sayama, H. Sugihara, Y. Abe, Chem. Lett. 34 (2005) 1122-1123.
8. J.B. Goodnough, R.N. Castellano, J. Solid State Chem. 44 (1982) 108-112.
9. P.P. Rao, S.J. Liji, K.R. Nair, Mater. Lett. 54 (2004) 1924-1927.
10. R.C. Ewing, W.J. Weber, J. Lian, J. Appl. Phys. 95 (2004) 5949-5971.
11. S. Pace, V. Cannillo, J. Wu, D.N. Boccaccini, S. Seglem, A.R. Boccaccini, J. Nucl. Mater. 341 (2005) 12-18.

12. K.G. Jasmeet, O.P. Pandey, K. Singh, *Int. J. Hydrogen energy* 37 (2012) 3857-3864.
13. A. Garbout, S. Bouattour, A.W. Kolsi, *J. Cryst. Growth* 307 (2007) 219-228.
14. Z.S. Chen, W.P. Gong, T.F. Chen, S.L. Li, *Bull. Mater. Sci.* 34 (2011) 429-434.
15. K.G. Jasmeet, O.P. Pandey, K. Singh, *Solid State Sci.* 13 (2011) 1960-1966.
16. A.F. Fuentes, K. Boulahya, M. Maczka, J. Hanuza, U. Amador, *Solid State Sci.* 7 (2005) 343-353.
17. T. Ting-ting, W. Li-Xi, Z. Qi-tu, *J. Alloys Compd.* 486 (2009) 606-609.
18. S. Kramer, M. Spears, H.L. Tuller, *Solid State Ionics* 72 (1994) 59-66.
19. R. Kant, K. Singh, O. P. Pandey, *Int. J. Hydrogen energy* 33 (2008) 455-462.
20. Z. Gao, Z. Mao, C. Wang, Z. Liu, *International Journal of Hydrogen Energy* 35 (2010) 12905-12910.
21. M.M. Yahyaoui, K. Limame, B. Jaber, A. Elghazouali, S. Sayouri, *International Review of Physics* 7 (2013) 393-399.
22. K. Limame, S. Sayouri, A. El Ghazouali, L. Hajji, T. Lamcharfi, B. Jaber, A. Housni, *Ferroelectrics* 371 (2008) 68-81.
23. N. Pailhé, M. Gaudon, A. Demourgues, *Mater. Res. Bull.* 44 (2009) 1771-1777.
24. E. Aleshin, R. Roy, *J. Am. Ceram. Soc.* 45 (1962) 18-25.
25. A.W. Sleight, *Inorg. Chem.* 7 (1968) 1704-1708.
26. P.J. Wilde, C.R.A. Catlow, *Solid State Ionics* 112 (1998) 173-183.
27. M. Maczka, J. Hanuza, K. Hermanowicz, A.F. Fuentes, K. Matsushira, Z. Hiroi, *J. Raman Spectrosc.* 39 (2008) 537-344.
28. W.J. von Becker, G. Will, *Zeitschrift für Kristallographie* 131 (1970) 278-288.
29. B.P. Singh, A.K. Parchur, R.K. Singh, A.A. Ansari, P. Singh, S.B. Rai, *Phys. Chem. Chem. Phys.* 15 (2013) 3480-3489.
30. S.L. Swartz, T.R. Shrout, *Mater. Res. Bull.* 17 (1982) 1245-1250.
31. O. Merka, D.W. Bahnemann, M. Wark, *Chem. Cat. Chem.* 4 (2012) 1819-1827.
32. A. Mesquita, M. I.B. Bernardi, C. Godart, P.S. Pizani, A. Michalowicz, V.R. Mastelaro, *Ceram. Int.* 38 (2012) 5879-5887.
33. K. Aykan, *J. Am. Ceram. Soc.* 51 (1968) 577-582.
34. M.C. Gelabert, R.A. Laudise, R.E. Riman, *J. Cryst. Growth* 197 (1999) 195-203.
35. H.C. Gupta, S. Brown, N. Rani, V.B. Gohel, *J. Raman Spectrosc.* 32 (2001) 41-44.
36. M.L. Sanjuán, C. Guglieri, S. Diaz-Moreno, G. Aquilanti, A.F. Fuentes, L. Olivi, J. Chaboy, *Phys. Rev. B* 84 (2011) 104207 1- 104207 18.
37. A. Garbout, A. Rubbens, R. N. Vannier, S. Bouattour, A. W. Kolsi, *J. Raman Spectrosc.* 39 (2008) 1469-1474.
38. S. Bouattour, D.P. Ferreira, A. Hamdi, L.F. Vieira Ferreira, A.M. Botelho do Rego, *Materials Chemistry and Physics* 138 (2013) 507-513.
39. W.L. Liu, H.R. Xia, H. Han, X.Q. Wang, *J. Cryst. Growth* 269 (2004) 499-504.
40. A. Garbout, I. Ben Taazayet-Belgacem, M. Férid, *J. Alloys Compd.* 573 (2013) 43-52.
41. V. Swamy, B. C. Muddle, Q. Dai, *Applied Physics Letters* 89 (2006) 163118-163120.
42. H. Cheng, J. Ma, Z. Zhao, L. Qi, *Chem. Mater.* 7 (1995) 663-671.
43. D. Bersani, P.P. Lottici, A. Montenero, S. Pignoni, G. Gnappi, *J. Mater. Sci.* 31 (1996) 3153-3157.
44. Y. Deng, Z. Yin, Q. Chen, M.S. Zhang, W.F. Zhang, *Mater. Sci. Eng. B* 84 (2001) 248-251.
45. T. Zhu, G. Han, Z. Ding, Z. Han, *J. Mater. Sci. Lett.* 15 (1996) 1747-1748.
46. A.M. Botelho do Rego, L.F. Vieira Ferreira, in "Handbook of Surfaces and Interfaces of Materials" (Academic Press, 2001) p. 275.
47. L.F. Vieira Ferreira, I.L. Ferreira Machado, *Current Drug Discovery Technologies* 4 (2007) 229-245.
48. R. Terki, G. Bertrand, H. Aourag, C. Coddet, *Physica B Condensed Matter* 392 (2007) 341-347.
49. W.R. Panero, L. Stixrude, R.C. Ewing, *Physical Review B* 70 (2004) 054110 1 - 054110 11.